Saturation of Laser Imprint on Ablatively Driven Plastic Targets

R. J. Taylor

Imperial College of Science, Technology and Medicine, London SW7 2BZ, United Kingdom

A. L. Velikovich

Berkeley Research Associates, Inc., Springfield, Virginia 22150

J. P. Dahlburg

Plasma Physics Division, Naval Research Laboratory, Washington, D.C. 20375

J. H. Gardner

LCP&FD, Naval Research Laboratory, Washington, D.C. 20375

The imprinting of areal density perturbations on thick planar plastic targets has been studied numerically and analytically. Simulations predict that the target modulation saturates while still in a small-amplitude regime. General scaling laws relating saturation times and amplitudes to mean laser drive and wavelength, and perturbation amplitude and wavelength, are summarized from the simulations. A linear gasdynamic model is used to study the physical mechanisms responsible for the saturation, and provides strong evidence that mass ablation is the dominant stabilizing influence. [S0031-9007(97)03946-X]

PACS numbers: 52.40.Nk, 52.35.Py

When a laser-driven inertial confinement fusion (ICF) pellet is imploded, the ablative Rayleigh-Taylor Instability (RTI) [1] produces exponential growth of any initial mass perturbations on the pellet. The seed for the ablative RTI is provided by limitations in target fabrication, and by the imprint [2–4] of inevitable spatial nonuniformities in the laser beams. If the laser has been optically smoothed, then the imprint can be very small, but it can never be completely eliminated and is generally larger than target nonuniformities resulting from the manufacturing process. This means that imprint is the dominant seed of the RTI in direct-drive ICF, and so understanding and control of the process is of paramount importance. During the majority of a laser-driven implosion the laser absorption region is radially farther out than the high-density ablation surface, and so the driving pressure nonuniformities are rapidly smoothed out by thermal conduction [5]. However, in the very early part of the laser pulse the plasma corona is thin, and nonuniformity of the laser beam has a larger effect on the target. Laser imprinting is thus primarily an impulsive effect whose duration is short compared to a shock transit time through the pellet shell.

Thermal smoothing stops the lateral *acceleration* of the material, but does nothing to remove the lateral *velocity* perturbation field already in place. Thus a situation akin to the Richtmyer-Meshkov instability (RMI) [6] can be expected, where the passage of a nonuniform shock perturbs an interface, and subsequent linear amplification of these perturbations is due to the velocity field thereby generated. However, a more complex phenomenon is observed in numerical simulations of laser imprinting. An early period of growth of the target mass perturbations is

followed by small amplitude saturation and subsequent decay. This is a clear indication that some stabilizing process is at work.

Both the early-time growth and the saturation of the areal mass perturbation amplitude δm in a laser-driven target have been observed numerically, in isolated instances [7], but there were no general scaling rules, and the saturation was not understood. In this Letter we present scalings for imprint from numerical simulations, and a plausible model to explain the observed δm saturation. The scalings apply over a wide range of conditions relevant to the direct-drive laser-fusion problem, and agree for the most part with those predicted by a linear analytical model similar to that describing the classical RMI [8]. Moreover, by means of comparison between the numerical and analytical results, we demonstrate for the first time that the small-amplitude saturation of δm is primarily due to mass ablation, which removes perturbed material from the unstable target surface. Although the importance of mass ablation for the RTI has been understood for many years [9], this is the first evidence of its relevance to early-time RMI-like mass imprinting.

The simulations reported here use the FAST code [10], which has previously proved effective at reproducing experimental observations of imprinting [3]. The code includes: FCT advection; inverse bremsstrahlung laser energy deposition; Spitzer-Härm thermal conduction; variable Eddington multigroup radiation transport with STA-NRL [11] opacities and tabulated Henke [12] opacities at low temperatures; and, a tabulated equation of state (EOS). In all cases, simulations are of semi-infinitely thick, planar polystyrene (CH) targets irradiated with a

laser beam modulated by a sinusoidal perturbation in a transverse (y) direction. There are at least twenty grid points per modulation wavelength in y, and the laser-direction axial (x) grid was designed such that $\delta x = 0.2$ μm from 5 μm in front of the ablation front through the entire ablation front region in the target.

The parameters that were independently varied in this study for each of the relevant laser wavelengths $\lambda_L = 0.249, 0.35,$ and 0.53 μm include: the mean laser intensity I_o from 1×10^{12} to 9×10^{13} W/cm^2; the laser spatial perturbation amplitude $\delta I/I$ from 0.5 to 10.0%; and, perturbation wavelengths λ_s typical of laser speckle scales, from 7.5 to 60 μm. Following an initial 250 ps linear ramp from 3×10^9 W/cm^2 to I_o, the irradiance is held constant in time. For a given run, both $\delta I/I$ and λ_s are also held fixed in time. The scalings reported here confirm many of those obtained with the hydrocode POLLUX [13,14]. The temporal scalings are also observed in ISI simulations, where laser perturbation amplitudes fluctuate statistically in y and t. The scalings are qualitatively independent of both the EOS and radiation transport details, and are computationally robust.

The extent of the laser imprinting is measured by the modulation in target areal density, $\delta m(t) = \delta[\int_{x_1}^{x_2} \rho(x, y, t)\, dx]$, where ρ is the mass density and $\delta[\,]$ denotes the y rms variation of the enclosed quantity. The point x_1 is far to the interior of the target, ahead of the shock front. The point x_2 is taken ~ 12 μm beyond the critical surface so as to include all significantly modulated plasma. The pressure perturbations δP at the ablation front are smoothed out by thermal conduction by about $t = 500$ ps. Long after that, the perturbation growth slows down until δm saturates and subsequently decays; see Fig. 1(a). This imprint saturation is not caused by the modulation entering a nonlinear regime, which is characteristic for both the RTI and the RMI. Rather, it is a linear, small-amplitude phenomenon. For all time through "saturation," $\delta m(t) \propto \delta I/I$ while the time scale is independent of $\delta I/I$. Therefore, the final amplitude

of saturation A_{sat} also varies linearly with the same quantity, whereas the saturation time t_{sat} is independent of it. This is illustrated by Fig. 1(b), which is a typical sample from our database. Thus, a reduction in the beam nonuniformity generates a corresponding reduction in the target imprint in all cases.

From our database of more than 200 simulations, we have generated a predictive saturation scaling law that agrees with the observed δm amplitude (A_{sat}, μm g/cm^3) and time (t_{sat}, ns) saturation values to an accuracy of better than $\sim 20\%$ on average for both t_{sat} and A_{sat}. These are

$$t_{\text{sat}} \simeq 0.06 \lambda_s^{1.1} I_0^{-3/8}, \tag{1}$$

$$A_{\text{sat}} \simeq 0.052 \lambda_s^{f_1} I_o^{f_2} \lambda_L^{f_3} \delta I/I, \tag{2}$$

with

$$f_i = \alpha_{i1} \lambda_s + \alpha_{i2} \lambda_L + \alpha_{i3} I_o + \alpha_{i4},$$

where the parameters in the scaling are as follows: perturbation wavelength (λ_s, μm); mean intensity (I_o, 10^{13} W/cm^2); laser wavelength (λ_L, μm); rms perturbation amplitude ($\delta I/I$); and, with coefficients $\alpha_{13} = -0.067$, $\alpha_{14} = 1.49$, $\alpha_{21} = 0.004$, $\alpha_{22} = -0.94$, $\alpha_{24} = 0.408$, $\alpha_{31} = 0.0037$, $\alpha_{33} = -0.07$, $\alpha_{34} = -1.13$, and α_{11}, α_{12}, α_{32}, and α_{23} all zero. The scaling law is a good fit, with errors exceeding 20% only for runs at the high-I_o, long-λ_s, and short-λ_L edges of the parameter space. In these equations t_{sat} is defined as the time just prior to saturation when the time derivative of δm is 0.1 of its maximum value, and A_{sat} is δm at that time. This definition reduces the statistical variation introduced by the sonic waves in the solution. In all cases, δm fully saturates, as can be seen by the representative curve, Fig. 1(a). The temporal saturation scaling, Eq. (1), is shown as a function of λ_s and I_o in Fig. 2. The t_{sat} dependence on I_o, $I_o^{-3/8}$, is approximately $P_a^{-1/2}$. A balance between the differences in mass ablation and thermal smoothing accounts for the lack of laser wavelength variation in Eq. (1). Figure 3 shows the scaling of
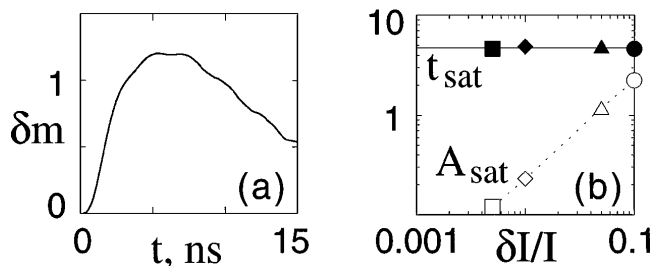
FIG. 1. Target areal density modulation, δm, for $I_o = 3 \times 10^{12}$ W/cm^2, $\lambda_s = 30$ μm and $\lambda_L = 0.249$ μm. (a) δm (μm g/cm^3) as a function of time, for rms $\delta I/I = 0.05$; (b) δm maximum as a function of rms $\delta I/I$. Saturation time t_{sat} in ns (solid line, symbols) is independent of $\delta I/I$, and saturation amplitude A_{sat} in μm g/cm^3 (dashed line and open symbols) varies directly as $\delta I/I$.
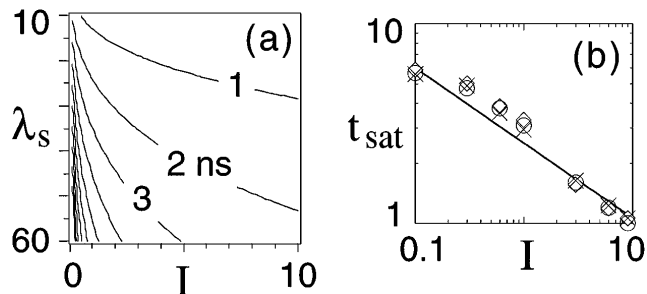
FIG. 2. Temporal δm saturation (ns) variation as functions of I_o (10^{13} W/cm^2) and λ_s (μm), for rms $\delta I/I = 0.01$. (a) Contour plot of Eq. (1); (b) Eq. (1) for $\lambda_s = 30$ μm. For (b), simulation datapoints overlay the Eq. (1) scaling curves for: 0.249 μm (crosses); 0.35 μm (circles); and, 0.53 μm (diamonds) λ_L.
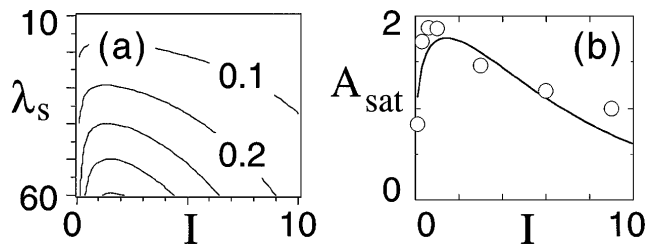
FIG. 3. Amplitude δm saturation (μm g/cm^3) variation as functions of I_o (10^{13} W/cm^2) and λ_s (μm), for $\lambda_L = 0.35$ μm. (a) Contour plot of Eq. (2), for rms $\delta I/I = 0.01$; and, (b) Eq. (2) scaling curve with simulation datapoints overlaid, for $\lambda_s = 45$ μm, and rms $\delta I/I = 0.05$.

$A_{\rm sat}$, Eq. (2), as a function of I_o and λ_s for the three laser wavelengths. Despite the complexity of the expression in Eq. (2), the essentially simple nature of the scaling is apparent from the contour plot, which is similar over the range of λ_L investigated. For the relevant parameter ranges considered, 1% KrF (0.249 μm), blue (0.35 μm), and green (0.53 μm) laser light imprint saturate at a maximum amplitude of about 0.7, 0.5, and 0.3 μm g/cm^3, respectively, with $t_{\rm sat}$ between 2 and 10 ns.

In order to investigate the influence of the various processes at work in imprinting, the problem was examined analytically with a gasdynamic model similar to that presented in [8]. Consider a half space filled with uniform ideal gas whose density is ρ_0. At time $t = 0$, a shock wave is driven into the gas by an ablative pressure P_a so that the shock propagates at constant speed D, compressing the gas to the density ρ_1. The velocity of the shock front with respect to the shocked material is thus $D_1 = \rho_0 D/\rho_1$. A single-mode pressure perturbation is imposed upon P_a at the ablation front: $\delta P[x = x_a(t), t] = \delta P_a f(t) \exp(iky)$, where $\delta P_a/P_a = 0.75\delta I/I$, and the decaying function $f(t)$ describes thermal smoothing as the corona develops. For this we use the expression $f(t) = \exp(-t/t_1)$, with $t_1 = 500$ ps, as taken from the simulation. The effect of mass ablation is modeled by removing the fluid particles from the ablation front at the velocity $v_a = \dot{m}/\rho_1$ relative to the fluid, where $\dot{m}$ [g/(cm^2 s)] is the mass ablation rate. The important parameter of the model with mass ablation becomes the ratio of the two velocities $\mu = v_a/D_1 = \dot{m}/\rho_0 D$ and $0 \leq \mu < 1$. The limiting case $\mu = 0$ corresponds to absence of mass ablation, whereas the larger μ, the more important $\dot{m}$ is. Values for μ are extracted from the simulation. In the simulation, the unperturbed axial ρ and P profiles are not flat and steady, as assumed in the model, so that the estimate of $\dot{m}$ should refer to a certain density level. For our baseline case (Fig. 4, solid line with closed circles), $D = 1.24 \times 10^6$ cm/s, and the mass flow rate through the surface $\rho = 1$ g/cm^3 is about 1.25×10^5 g/(cm^2 s), hence $\mu \approx 0.1$. Choosing ρ closer to the actual value of $\rho_1 = 2.5$ g/cm^3 would increase the effective value of μ up to 0.2–0.3.
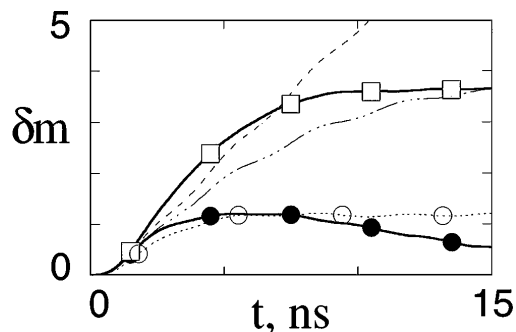
FIG. 4. Time evolution of δm (μm g/cm^3) for $P_a = 1$ Mbar ($I_o = 3 \times 10^{12}$ W/cm^2 for simulations), rms $\delta I/I = 0.05$, $\lambda_s = 30$ μm, and $t_1 = 0.5$ ns from: simulations: with radiation transport (solid line with solid circles); without radiation transport (solid line with squares); and, by the gasdynamic model for the same conditions and: $\mu = 0$ (dashed line); $\mu = 0.1$ (chain-dashed line); and, $\mu = 0.3$ (dotted line with open circles).

The linearized perturbation problem is solved analytically as in [8] for the classical RMI. In Fig. 4, the analytical results for δm are compared to the simulation. Without $\dot{m}$ ($\mu = 0$) the model predicts typical RM behavior—unlimited linear growth of δm, with superimposed sonic oscillations. However, the late time evolution is qualitatively different with $\dot{m}$ included, in that the model predicts saturation of δm, as observed in the simulations. To explain it, we note that, in the absence of lateral pressure gradient, the linear growth of the RM-like instabilities is essentially due to vorticity ω, both initially deposited at the interface and generated by the rippled shock front; see [8,15]. Since the fluid particles carrying ω are constantly removed from the flow through the ablation front, and ω production at the shock front decreases as the ripples decay, the shock-compressed plasma at the ablation front eventually becomes irrotational, stopping the perturbation growth. Both the model $A_{\rm sat}$ and $t_{\rm sat}$ agree well with the simulation, although the decay after saturation is not observed. These discrepancies result from the omission of a vortical flow effect similar to that described in [10]. The early-time δP accelerates the plasma in the lateral direction, producing ω that supports lateral motion long after the lateral pressure gradient is smoothed out. This motion generates a more intense downstream axial plasma outflow through the pressure valleys. In both cases of classical RMI and RTI, the mass is driven laterally from the bubble area and then falls axially into the spike, increasing areal mass. In our case, however, the mass driven to the spike (pressure valley) is lost from there at higher rate through the outer boundary of the δm integration surface. Thus δm decays instead of growing, and the bubble-spike structure flattens instead of sharpening. Our analytical model does not account for the lateral nonuniformity of effective $\dot{m}$, nor for the vortical flow in the low-density plasma. It describes only the effect of lateral mass redistribution in

the dense plasma and predicts its saturation solely due to the uniform loss of the ω-carrying fluid particles. For the conditions of Fig. 4, the nonuniformity of the axial mass losses and the vortical flow of the low density mass from spike to bubble, which both act to decrease the rms δm, are responsible for the decay of δm.

Some of the scalings mentioned above can be explained by the gasdynamic model. In the linear theory, all the perturbations are proportional to the external driving perturbation, that is, to $\delta I/I$. The only time scale in the linear theory is λ_s/D, hence t_{sat} varies as λ_s, all other parameters being constant. Since in the relevant range of the parameter μ, the dimensionless t_{sat} is relatively insensitive to the choice of values of μ and t_1, and for strong shock waves P_a scales as $\rho_0 D^2$, we conclude that t_{sat} scales as $P_a^{-1/2}$, in general agreement with the simulation results.

In summary, saturation of laser imprinting has been observed in single-mode imprint simulations across a broad range of parameters relevant to ICF. In this Letter we have summarized the saturation scalings in approximate scaling laws, and we have used a highly idealized model of the flow to demonstrate that $\dot{m}$ is the fundamental hydrodynamic mechanism which produces the numerically observed imprint stabilization. This mechanism is the same as that which provides reduction to the rate of the ablative RTI [9]. In neither case is the ablation front really a contact surface formed by a fixed set of the fluid particles, but instead is a surface through which mass ablates. With a constant outflow of the perturbed fluid particles, continuous perturbation growth requires additional energy. In the case of the RTI, the acceleration, or effective gravity, provides such an energy source, and $\dot{m}$ generally serves to reduce the ablative RT growth rate by a term proportional to the wave number [9]. However, the RMI, in contrast to the RTI, develops without any permanent energy source. Thus, introducing an outflow of perturbed fluid particles provides a permanent sink for energy (and ω, see above), which results in full saturation of perturbation growth for all wavelengths. We note that the same stabilizing mechanism stops the RM-like perturbation growth in planar targets with surface ripples [16] and would saturate the perturbation growth due to initial target nonuniformity. In the simulations, thermal and radiative heat conduction both contribute to increasing the effects of saturation by effectively increasing $\dot{m}$. However, the fundamental result, that δm saturates in a finite time, is independent of such particulars, as is demonstrated by Fig. 4. We have verified that the contribution of those mechanisms is to shape the axial ρ and P profiles rather than to damp the perturbation directly. Generically,

both t_{sat} and A_{sat} are determined by a finite surface layer within a finite time interval. This provides us with an interesting concept that may prove extremely useful in the development of an ablator for high-gain direct-drive laser fusion, i.e., mass ablation is the dominant control parameter in the problem of laser imprinting.

[1] J. Nuckolls et al., Nature (London) **239**, 139 (1972); D. H. Sharp, Physica (Amsterdam) **12D**, 3 (1984).

[2] R. G. Evans et al., Phys. Rev. Lett. **49**, 1639 (1982); M. H. Emery et al., Phys. Fluids B **3**, 2640 (1991).

[3] R. J. Taylor et al., Phys. Rev. Lett. **76**, 1643 (1996); C. J. Pawley et al., Phys. Plasmas **4**, 1969 (1997).

[4] J. L. Bocher et al., Phys. Rev. Lett. **52**, 823 (1984); M. Desselberger et al., Phys. Rev. Lett. **68**, 1539 (1992); D. H. Kalantar et al., Phys. Rev. Lett. **76**, 3574 (1996); S. G. Glendinning et al., Phys. Rev. E **54**, 4473 (1996).

[5] K. A. Brueckner and S. Jorna, Rev. Mod. Phys. **46**, 325 (1974); S. E. Bodner, J. Fusion Energy **1**, 221 (1981).

[6] R. D. Richtmyer, Commun. Pure Appl. Math. **13**, 297 (1960); E. E. Meshkov, Fluid Dyn. **4 (5)**, 101 (1969).

[7] M. Desselberger et al., Phys. Rev. Lett. **65**, 2997 (1990); **74**, 2961 (1995).

[8] A. L. Velikovich, Phys. Fluids **8**, 1666 (1996).

[9] S. E. Bodner, Phys. Rev. Lett. **33**, 761 (1974); H. Takabe et al., Phys. Fluids **28**, 3676 (1985).

[10] M. H. Emery et al., Appl. Phys. Lett. **41**, 808 (1982); J. P. Dahlburg et al., J. Quant. Spectrosc. Radiat. Transf. **54**, 113 (1995).

[11] A. Bar-Shalom et al., Phys. Rev. A **40**, 3183 (1989).

[12] B. L. Henke et al., At. Data Nucl. Data Tables **54**, 181 (1993).

[13] G. J. Pert, J. Comput. Phys. **43**, 111 (1981).

[14] R. J. Taylor, Ph.D. thesis, University of London, 1996.

[15] J. G. Wouchuk and K. Nishihara, Phys. Plasmas **4**, 1028 (1997).

[16] T. Endo et al., Phys. Rev. Lett. **74**, 3608 (1995); R. Ishizaki and K. Nishihara, Phys. Rev. Lett. **78**, 1920 (1997).